THE JOURNAL OF PHYSICAL CHEMISTRY C
A JOURNAL OF THE AMERICAN CHEMICAL SOCIETY

pubs.acs.org/JPCC
Article

Cu-Doped SnO_2 Nanocrystals: Tunable Magnetism, Critical Incorporation Limit, and Defect Configuration Analysis by EPR and *Ab Initio* DFT

L. Villegas-Lelovsky, F. F. H. Aragón,* P. C. Morais, D. G. Pacheco-Salazar, P. E. N de Souza, J.A.H. Coaquira, and Ricardo Paupitz

Cite This: *J. Phys. Chem. C* 2026, 130, 1257−1270

ABSTRACT: Copper in oxide semiconductors exhibits distinct electronic and magnetic behavior depending on its oxidation state, with Cu^{1+} acting as a nonmagnetic impurity and Cu^{2+} contributing to the magnetic moment. In SnO_2, Cu incorporation represents a heterovalent substitution for Sn^{4+}, which inherently promotes formation of compensating defects, particularly oxygen vacancies, that can strongly influence electronic and magnetic properties. To elucidate these effects, we investigated Cu-doped SnO_2 nanocrystals through combined experimental and theoretical approaches. Electron paramagnetic resonance (EPR) revealed that Cu incorporation of up to 3% enhances resonance intensity, consistent with isolated Cu^{2+} ions in the SnO_2 matrix. Beyond 3%, the EPR signal intensity decreases, and hyperfine parameters stabilize due to Cu^{2+} clustering and spin−spin interaction. Magnetization measurements revealed a paramagnetic phase (reflecting the presence of isolated Cu^{2+}) that coexists with a ferromagnetic phase attributed to bound magnetic polarons and magnetic clustering. Complementary first-principles calculations showed that Cu substitution modifies the electronic structure by introducing localized density of states variations and altering the spin−charge density distribution, particularly near oxygen vacancies. Deeper in-plane defects were found to stabilize magnetization, whereas surface defects promoted competing ferromagnetic and antiferromagnetic interactions. Structural characterization by X-ray diffraction and morphological analysis using high-resolution transmission electron microscopy further confirmed lattice compression and particle size reduction with increasing Cu-content. The calculated and experimental findings provide a comprehensive and interconnected understanding, not yet emphasized in the literature, of the interplay among defects, doping, and magnetism in Cu-doped SnO_2.

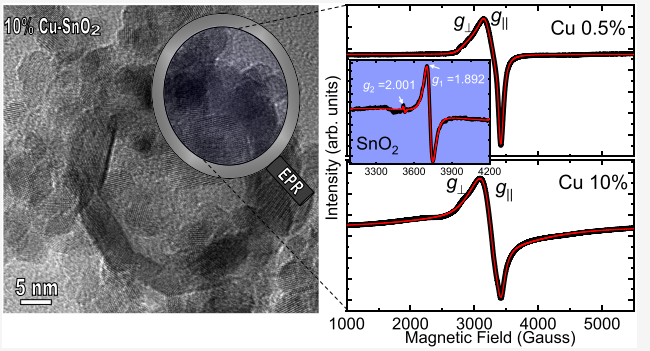

I. INTRODUCTION

Diluted magnetic semiconductors (DMS) are materials that blend semiconductor and nonzero magnetic moment of doping ions. These materials consist of a nonmagnetic semiconductor host, such as GaAs or ZnO, doped with a small amount of magnetic impurities. These impurities often include transition metals (TMs) like Fe, Co, and Ni, as well as rare earth (RE) elements such as Er, Tb, and Dy. The defining physical characteristic of DMS is the exchange interaction between dopants' localized magnetic moments and itinerant carriers (electrons or holes) of the host matrix. This interaction generates significant magnetic effects, a notable example of such effects can be observed in $Cd_{1-x}Mn_xSe$ quantum dots.[1] DMS have garnered significant interest due to their potential applications in spintronics, a field that strives to leverage the spin degree of freedom of electrons, in addition to their charge. Unlike classical magnetic semiconductors, such as RE chalcogenides, diluted magnetic semiconductors are characterized by the intentional dilution of the magnetic element. This deliberate modification distinguishes DMS from traditional magnetic semiconductors.[2−5]

In 2000, room-temperature ferromagnetism (RTFM) was predicted in 5% Mn-doped GaN and ZnO,[6] which represents a significant milestone in establishing magnetic order for practical applications. Subsequently, numerous studies have reported achieving RTFM by doping with various TM elements.[7] Many research groups have reported the presence of RTFM in pure and nonmagnetic ion-doped materials, indicating a possible relationship between magnetism and lattice defects.[8,9] This finding challenges the conventional

Received: August 10, 2025
Revised: October 15, 2025
Accepted: October 16, 2025
Published: November 5, 2025

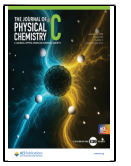

https://doi.org/10.1021/acs.jpcc.5c05607
J. Phys. Chem. C 2026, 130, 1257−1270

understanding of magnetic order in insulators requiring d or f electrons in a specific part of the cation's shell. As a result, several research teams have explored the origins of the experimentally observed d^0 RTFM. These studies have shown that defects can introduce traveling carriers that play a crucial role in magnetic coupling.[10] Some scholars proposed that the presence of oxygen vacancies or defects due to interface mismatch stress between thin film and substrate may result in ferromagnetism in nonmagnetic oxides like TiO_2, ZnO, and SnO_2.[11−13] To date, various intrinsic defects, including structural and surface defects, as well as strain and point defects like vacancies and interstitials, have been found to cause RTFM in oxide semiconductors.[14−16] Nonetheless, the source of d^0 magnetism remains a topic of debate. Because native defects in oxide semiconductors are highly sensitive to preparation methods and protocols, the lack of reliability and reproducibility in experimentally observed d^0 magnetism continues to be an unresolved issue. Therefore, a more controllable approach for introducing defects into crystal materials is crucial to unveil the mechanism of ferromagnetism caused by lattice defects. Experimentally, the emergence of magnetic response in semiconducting metal oxides, such as SnO_2, has been observed when doped with low concentrations of TMs like Ni, Cr, and Fe,[17−19] or RE elements such as Er and Dy.[20,21] In these studies, RTFM is consistently observed only at low doping concentrations, and the possibility of secondary impurity formation contributing to this effect was conclusively ruled out. Besides, a consensus in the literature suggests that oxygen vacancies play an active role in the ferromagnetic response, which becomes more pronounced under oxygen-deficient conditions.[22,23] This behavior highlights a specific signature of defect-induced magnetic ordering: ferromagnetism typically emerges at low dopant concentrations and is strongly correlated with a high density of structural defects.[24]

The magnetic properties of Cu ions in SnO_2 hosting material, in bulk and surface periodic geometries, were systematically and theoretically investigated in the present report. Different effects on the bulk and slab materials for similar point defect configurations were observed. The (110) preferential direction was deliberately chosen in the present study, as it has been shown to be the most active direction, in both experimental and theoretical previous studies,[25−30] while addressing electronic properties due to the evolution of oxygen vacancies upon increasing the annealing temperature.

This review is organized as follows: In Section II, the theoretical approach details are presented, endorsed by ab initio calculations employed to determine the most likely defects, including their electronic and magnetic properties. In Section III, the synthesis and experimental characterization techniques are described. The main theoretical and experimental results are shown in Sections IV and V, respectively.

II. THEORETICAL APPROACH AND COMPUTATIONAL DETAILS

Calculations based on *ab initio* density functional theory (DFT)[31,32] were performed, in the framework of Quantum ESPRESSO suite package[33−35] version 6.8. For the exchange and correlation energy functional, investigations using the parametrized Perdew, Burke, and Ernzerhof (PBE)[36,37] lead to an accurate description of both geometry and electronic band structure. The Kohn−Sham equations were solved using the ultrasoft pseudopotential (USPP) basis,[38,39] by employing the following projectors $Sn(5s^15p^24d^3)$, $O(2s^12p^2)$, and $Cu(4s^14p^23d^3)$, where the valence orbitals are shown in parentheses. Atomic forces optimizations and the equilibrium volume of the SnO_2 unit cell were found by minimization of the stress tensor, employing a plane wave basis with a kinetic energy cutoff of 60 Ry. Meanwhile, the charge density was truncated at a cutoff energy of 480 Ry for the three-dimensional (3D) periodic bulk structures to avoid self-interaction between the periodic images with defects. A 2 × 2 × 3 supercell (24 Sn and 48 O atoms) with fixed lattice vectors was adopted for the 3D bulk structures. To avoid partial state occupation, a small Gaussian smearing of 0.027 eV was employed in all investigations. Moreover, electronic self-consistency was achieved with a tight convergence threshold criteria (1.36×10^{-9} eV) within the Kohn−Sham scheme, and equilibrium geometries were reached when all forces were smaller than 0.0250 eV/Å on every atom. For the Cu-doped supercell calculations, the collinear spin polarization was adopted. Aiming to investigate localized magnetic moments, the spatial resolved spin-charge density, $\Delta\rho(\mathbf{r}) = \rho_{\uparrow}(\mathbf{r}) - \rho_{\downarrow}(\mathbf{r})$, was employed.

III. EXPERIMENTAL DETAILS

DMS Cu^{2+}-doped SnO_2 nanoparticles (NPs) were synthesized via the polymeric precursor method (Pechine method).[40] This involved creating a polymer-based precursor containing copper and tin ions. Tin(II) chloride dihydrate ($SnCl_2{\cdot}2H_2O$, >98%, Scharlau), copper(II) nitrate trihydrate ($Cu(NO_3)_2{\cdot}3H_2O$, 99.5%, Merck), ethylene glycol ($C_2H_6O_2$, Delta quimica), and citric acid ($C_6H_8O_7$, >99.5, Delta quimica) were employed in the polymer precursor method to synthesize undoped and Cu-doped SnO_2 nanocrystals. Reagents were used as received without any further purification. The Cu-content was adjusted according to the atomic ratio Cu/(Cu + Sn), where x mol of copper (from $Cu(NO_3)_2{\cdot}3H_2O$) was mixed with $(1 - x) \times$ Eff mol of SnO_2 resin, with Eff representing the resin efficiency. The process began by dissolving citric acid in water, followed by the addition of aqueous solutions of $SnCl_2{\cdot}2H_2O$ and $Cu(NO_3)_2{\cdot}3H_2O$. Upon dissolution, Sn^{2+} and Cu^{2+} ions were released into solution. Citric acid acted as a chelating agent, coordinating with the as-dissolved metal cations to form stable metal−citrate complexes. Ethylene glycol was then added, promoting polyesterification with the metal−citrate complexes and leading to the formation of a homogeneous, transparent gel that ensured uniform metal distribution. Subsequently, a thermal treatment was carried out up to 500 °C for 12 h at a heating rate of 10 °C/min. As the temperature increased from room temperature, several decomposition steps occurred, and a stable crystalline phase was obtained at 500 °C, as confirmed by X-ray diffraction (XRD). More details of the synthesis protocol are available in a previous report.[41] Subsequently, XRD measurements were performed using a Rigaku MiniFlex 600 X-ray diffractometer equipped with Cu Kα radiation (λ = 1.5418 Å) and scanning in a 2θ range of 20−80°. Transmission electron microscopy (TEM) images were captured using a Talos F200i commercial microscope. Magnetic measurements were conducted using a commercial superconducting quantum interference device (SQUID) magnetometer (Quantum Design) within the temperature range of 5−300 K, while applying magnetic fields up to ± 70 kOe. Room-temperature electron paramagnetic resonance (EPR) measurements were carried out using a high-sensitivity Bruker ESP-300 spectrometer. EPR characterization of Cu-doped SnO_2 nanoparticles was performed with electromagnetic radiation at the

https://doi.org/10.1021/acs.jpcc.5c05607
J. Phys. Chem. C 2026, 130, 1257−1270

X-band microwave frequency (~9.75 GHz). For a summary of the experimental process, see the flowchart in Figure 1.

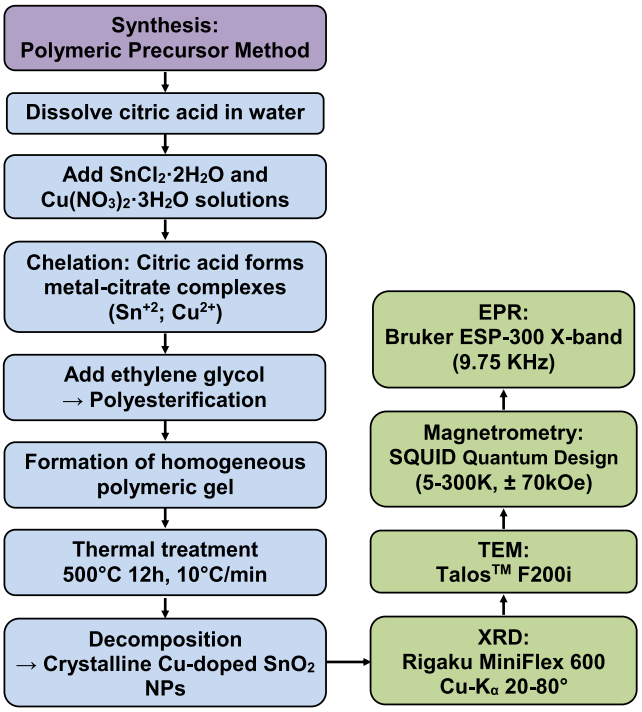

Figure 1. Flowchart illustrating the synthesis and characterization of Cu^{2+}-doped SnO_2 nanoparticles using the polymeric precursor method. The process includes precursor preparation, gel formation via chelation and polyesterification, thermal treatment for crystallization, and subsequent characterization by XRD, TEM, SQUID magnetometry, and EPR spectroscopy.

IV. THEORETICAL RESULTS

Our study systematically investigates the role of surface and subsurface defects and their impact on magnetic properties, focusing on the main preferential direction (110) plane, analyzed through the local density of states (LDOS) and spin-charge density difference (SCHDD). The LDOS isosurface gives insight into where electronic states are spatially localized, which is important for understanding the orbital topology changes on surfaces or interfaces. Meanwhile, the SCHDD isosurfaces reveal the magnetic polarization induced by the impurity on the surrounding impurity atom. These surfaces extend slightly to neighboring atoms, indicating spin delocalization or exchange interactions.

Figure 2 presents the atomic structure and electronic properties of SnO_2 with a single substitutional Cu impurity, corresponding to a doping level of 4.2%. Figure 2(a1−a3) shows Cu replacing a Sn atom in three distinct configurations: (a1) on the surface (top in-plane) without an oxygen vacancy, (a2) on the surface with a neighboring oxygen vacancy, and (a3) on a deeper in-plane site. Oxygen, tin, and copper atoms are colored red, gray, and blue, respectively. When a Cu ion substitutes for a Sn atom in the type I point defect scenario of the two-dimensional (2D) periodic system, as shown in Figure 2(a1), a Cu−O−Sn bridge appears in the outermost atomic plane. The Cu ion distorts the local electrical environment of the nearby outermost atoms by causing an imbalance in their DOS (Figure 2(b1)). Although the oxygen atoms at the surface show notable magnetization evidenced by the majority spin-up density surfaces, there is a small but non-negligible spin-down contribution, which partially counteracts the overall ferromagnetic behavior. This subtle interplay between magnetization of oxygen and Cu-induced electronic imbalance highlights the complex magnetic and electronic interactions at the surface of the SnO_2 structure (Figure 2(c1)). For type II defect (Figure 2(a2)), from the previous configuration, we have extracted the bridging oxygen atom (Cu-V_O-Sn). The lattice distortion near the oxygen vacancy significantly alters the bonding environment and the electronic states around the Cu ion, as reflected in LDOS (Figure 2(b2)). This distortion induces a spin-up majority density at the surface, as evidenced by the magenta isosurfaces in the SCHDD plot (Figure 2(c2)), where the oxygen vacancy amplifies surface magnetization as compared to the type I defect.

In the type III defect (Figure 2(a3)), where copper is located in the innermost atomic plane (deep in plane or bulk), the surface states remain largely unaffected (Figure 2(b3)). However, the SCHDD plot reveals balanced spin-up and spin-down density contributions to the magnetic ordering in the Cu-containing plane, while the spin-down majority density dominates at the outermost atomic plane before the vacuum (Figure 2(c3)). The deeper placement of Cu in the structure promotes a surface magnetization among the slab atoms, unlike what is observed in the 3D bulk case, as the uppermost oxygen atoms slightly enhance this spin alignment. Supporting Information: SCHDD of the SnO_2 bulk structure with one Cu atom and one oxygen vacancy (Figure S1).

To further investigate the role of the impurity concentration and spatial configuration, we examined two substitutional Cu atoms (8.3%) embedded within the SnO_2 slab, as shown in Figure 3. Three representative geometries were considered: (a1) Cu atoms placed in the same deep in-plane layer (denoted *dIp*); (a2) Cu atoms distributed across (110)-parallel planes—one at the surface, the other at a deeper site without an oxygen vacancy; and (a3) a similar parallel-plane configuration but with an oxygen vacancy adjacent to the deeper Cu atom.

The corresponding LDOS maps, shown in Figure 3(b1−b3), provide insight into the spatial redistribution of electronic states. In the *dIp* configuration (b1), the LDOS is predominantly localized around the Cu sites and neighboring oxygen atoms, suggesting that the substitutional Cu atoms perturb the local bonding environment without significantly altering the deeper electronic states of the slab. The spatial confinement of the electronic density indicates weak hybridization between the Cu sites, which is consistent with their close proximity. In contrast, the parallel-plane geometries (b2 and b3) reveal more delocalized features. In particular, the presence of an oxygen vacancy in (b3) promotes a redistribution of the electronic density, enhancing the delocalization of states and enabling stronger coupling between impurities and the host lattice.

The SCHDD plots in Figure 3(c1−c3) highlight the magnetic consequences of these configurations. In the *dIp* case (c1), a minority spin polarization remains confined to the immediate vicinity of the in-plane Cu atoms, reflecting a weak magnetic contribution outside this region. However, in the parallel-plane geometries (c2 and c3), a more extended and intricate spin-polarized region emerges. In (c2), spin polarization bridges form between Cu atoms, indicating cooperative alignment mediated through the lattice. Configuration (c3),

https://doi.org/10.1021/acs.jpcc.5c05607
J. Phys. Chem. C 2026, 130, 1257−1270

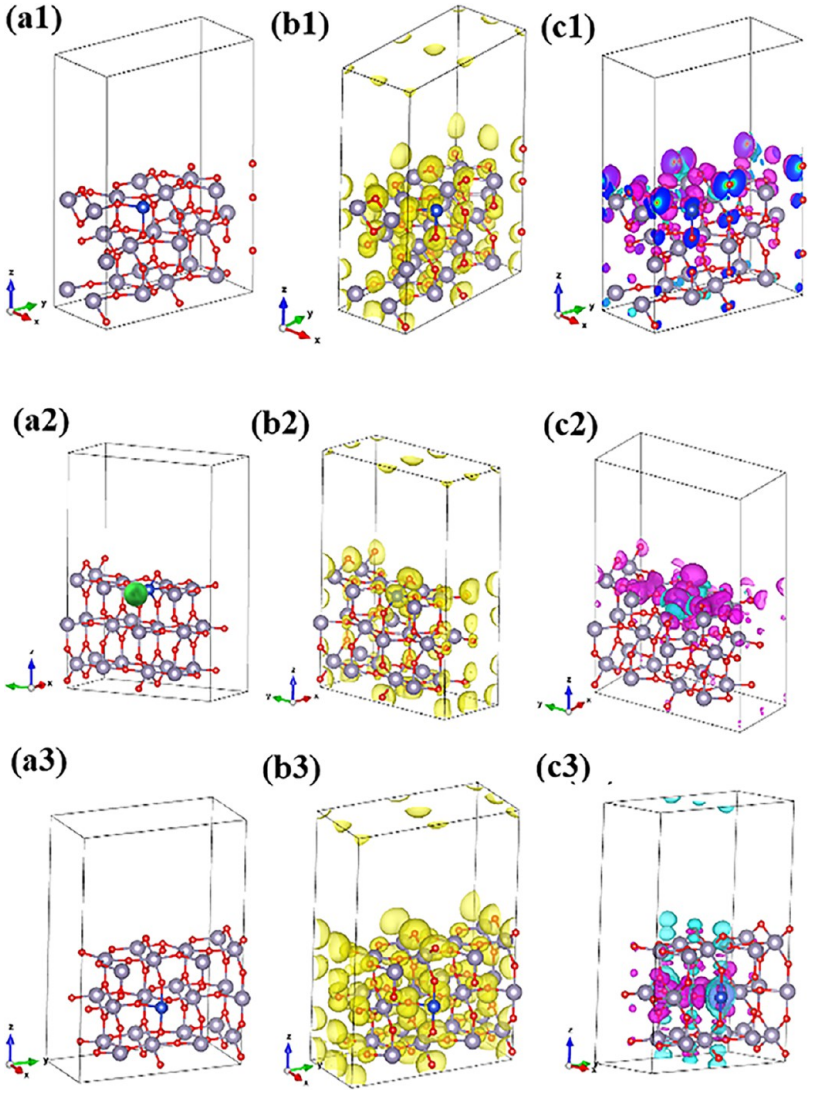

Figure 2. 2D bulk structures with one substitutional Cu atom top in plane (*tIp*), top in plane with oxygen vacancy (1 Cu_{Sn}(*tIp*) + 1 V_o), and deep in plane (*dIp*), (a1−a3), respectively, and corresponding local density of states (LDOS), (b1−b3) and spin-charge density difference (SCHDD), (c1−c3). The oxygen vacancy is marked by a green sphere in (a2). The isosurfaces values are 0.001 (magenta color) and −0.001 (cyan color), respectively.

incorporating an oxygen vacancy, exhibits the most pronounced and spatially extended spin polarization. The vacancy acts as a mediator of magnetic interaction, enabling long-range spin alignment potentially through enhanced exchange interactions and superexchange mechanisms.

These findings highlight the sensitivity of magnetic behavior to both impurity spacing and the local defect structure. When Cu atoms are placed in close proximity, the resulting magnetic moment is diminished due to the reduced polarization overlap. Conversely, with increased Cu−Cu separation (approximately 0.929 nm) and the presence of an intervening oxygen vacancy, a significantly enhanced magnetization is observed.

This effect is attributed to stronger exchange interactions and a vacancy-mediated spin alignment across the lattice. Altogether, our results demonstrate the tunability of the electronic and magnetic response of SnO_2 through impurity engineering and defect manipulation, providing a pathway toward the design of tailored magnetic oxide systems.

Table I provides a detailed summary of the key magnetic properties observed in the studied systems. Notably, the configuration featuring a single copper atom substitution combined with an oxygen vacancy (1 Cu_{Sn}(*tIp*) + 1 V_o) exhibits a significantly enhanced magnetic moment compared to its counterpart without the vacancy (1 Cu_{Sn}(*tIp*)). This observation highlights the critical role of oxygen vacancies in tuning the magnetic behavior of the material. Furthermore, a clear spatial dependence emerges: defects located deeper within the structure (1 Cu_{Sn}(*tIp*)) tend to exhibit magnetic moments closer to those of the bulk phase. This trend highlights the interplay between the defect depth and magnetic response, emphasizing the pronounced influence of surface proximity on the overall magnetic properties of the system.

Furthermore, the slab containing two copper ions in the same subsurface atomic plane, as illustrated in Figure 3(a1), exhibits spin polarizations both within and beyond this plane. However, it presents a lower total magnetization as compared to the defects located in separate planes.

Notably, the introduction of an oxygen vacancy near two copper ions, as depicted in Figure 3(a3), leads to a substantial increase in the overall magnetization, as shown in Table I. This

https://doi.org/10.1021/acs.jpcc.5c05607
J. Phys. Chem. C 2026, 130, 1257−1270

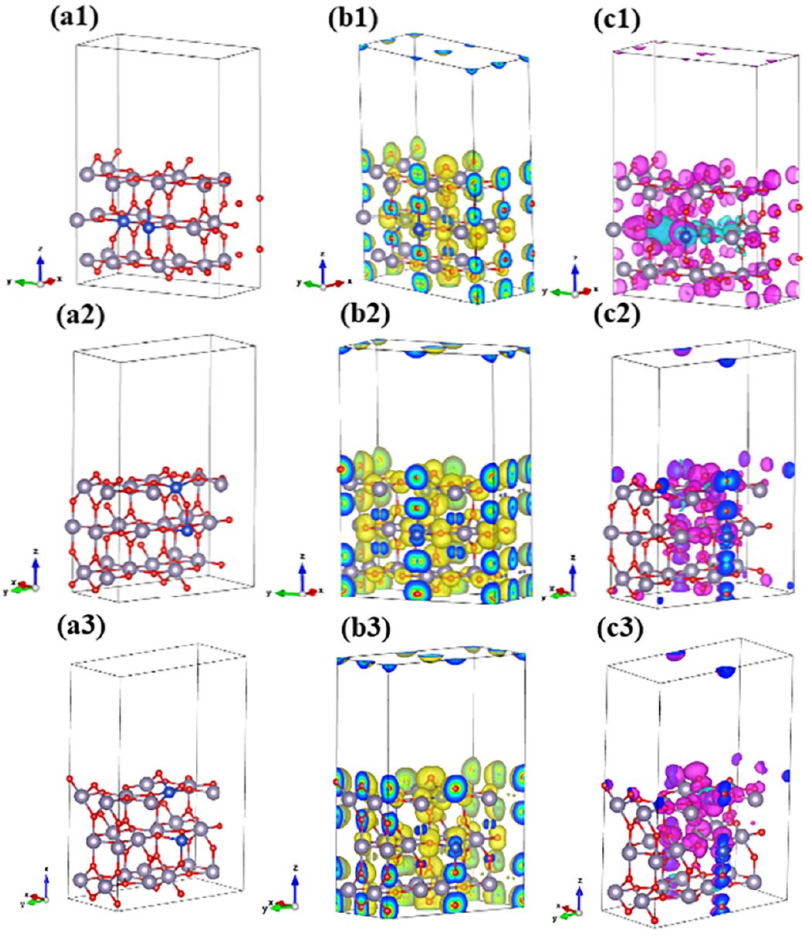

Figure 3. 2D bulk structures with two substitutional Cu atoms, within deep in plane (*dIp*) (a1), and belonging to the two neighboring planes (*pp*), one in the surface and other in subsurface plane (a2), and corresponding local density of states (LDOS) (b1, b2), and spin-charge density difference (SCHDD) (c1, c2).

Table I. Total Magnetization (M_T), Expressed in Units of Bohr magneton per atom (μ_B/Atom) for Each 2D Periodic Defect[a]

Cu-content (mol %)	structure	M_T (μ_B/atom)
4.2	1 Cu_{Sn}(*tIp*)	0.76
4.2	1 Cu_{Sn}(*tIp*) + 1 V_o	0.89
4.2	1 Cu_{Sn}(*dIp*)	1.00
8.3	2 Cu_{Sn}(*dIp*)	1.00
8.3	2 Cu_{Sn}(*pp*)	1.77
8.3	2 Cu_{Sn}(*pp*) + 1 V_O	2.00

[a]The notation used is as follows: *tIp* refers to top in plane, *Ip* indicates in plane, *dIp* denotes deep in plane, and *pp* represents the interplane configuration of the Cu atoms.

observation aligns with calculations for a single copper atom combined with one oxygen vacancy.

Among the different scenarios presented in Table I (visualized in Figures 2 and 3), leading to total magnetization (M_T) calculations, the 1 Cu_{Sn} (*dIp*) and 2 Cu_{Sn} (*dIp*) configurations, occurring respectively at 4.2 and 8.3% Cu-content, deserve special attention. It is worthy of note that the two scenarios provide similar values for the total calculated magnetization, namely, one Bohr magneton per atom. This theoretical finding, which aligns well with experimental data presented later on in this report, suggests that the deep in-plane (*dIp*) positioning of Cu atoms is more likely to occur.

To analyze the impact of magnetic impurities on the electronic structure of the metal oxide slab, we examined the spin-resolved projected density of states (PDOS) mapped onto the electronic band structure along the high-symmetry path Γ−Y−M−X−Γ, as shown in Supporting Information: 3D heat-map of total-, spin-up, and spin-down DOS projected on the band structure (Figure S3), for the case of one copper impurity. Visualization of the heat-map enables a clear identification of the orbital contributions and spin polarization effects induced by the copper ion.

In general, the spin-up and spin-down components of the Cu 4*s* and 4*p* states display minimal differences, indicating a negligible degree of spin polarization in these orbitals. In contrast, the Cu 3d orbitals exhibit a pronounced spin-dependent asymmetry near the Fermi level, signaling the presence of localized magnetic moments and impurity-induced exchange splitting. This behavior is consistent with the spatial spin density difference isosurfaces presented in Figure 2, which show magnetic polarization localized around the impurity and extending slightly into the surrounding lattice.

The emergence of spin-polarized 3d states near the Fermi energy suggests a significant hybridization between the impurity and host states, confined primarily to the surface region. Such localized magnetic features can play a critical role in mediating surface reactivity and magnetic coupling, especially in systems relevant for catalytic and spintronic applications.

https://doi.org/10.1021/acs.jpcc.5c05607
J. Phys. Chem. C 2026, 130, 1257−1270

To further elucidate the role of broken symmetry in the slab geometry, we analyzed the projected density of states (PDOS) on the band structure along the high-symmetry path Γ−Y−M−X−Γ, as shown in the Supporting Information: 3D heatmap of total-, spin-up, and spin-down DOS projected on the bands structure for the slab with two copper ions (Figure S4). The top row presents the total, spin-up, and spin-down PDOS; the middle and bottom rows depict the individual contributions from the Cu − 1 and Cu − 2 atoms, respectively. Notably, unlike the 3D bulk configuration (Supporting Information: 3D bulk structure with two substitutional Cu atoms, Figure S2), where the equivalence of Cu sites is preserved by lattice symmetry—the slab configuration breaks this symmetry and introduces site-specific electronic features.

The PDOS maps reveal that Cu − 1 and Cu − 2 contribute differently to the valence band structure. Cu − 1 exhibits more localized contributions around midvalence energies, whereas Cu − 2 displays broader, spin-polarized features extending toward the Fermi level, especially in the spin-up channel. This disparity highlights the impact of reduced dimensionality and inequivalent local environments within the slab, which allow impurity-specific electronic behavior to manifest. The enhanced exchange splitting associated with Cu − 2 further supports the emergence of site-dependent magnetism, reinforcing the relevance of dimensional confinement and surface terminations in governing the spin and charge landscapes of doped transition-metal oxides.

These results show the sensitivity of the electronic structure to defect-induced perturbations and highlight the importance of orbital-resolved analyses in understanding the microscopic origin of impurity-driven phenomena in complex oxides.

V. EXPERIMENTAL RESULTS

V.I. Structural and Morphological Characterization.

In Figure 4(a), the XRD pattern of the powders reveals the existence of a pure tetragonal rutile-type SnO_2 phase (JCPDS card, 41−1445; space group, $P42/mnm$) in all samples. Remarkably, the primary reflection is prominently evident along the (110) plane in the nanoparticle samples. This observation suggests that the characteristics of the (110) plane are preserved at the surface of the nanoparticles' counterparts, aligning with the dominant features observed in bulk systems.

To provide deeper structural insights, Rietveld refinement was employed to accurately extract the lattice parameters (a and c), average crystallite size ($\langle D \rangle$), and mean residual strain ($\langle \varepsilon \rangle$). The XRD peak profiles were modeled using a Lorentzian function, and the full width at half-maximum (β) was corrected for instrumental broadening according to $\beta_{corrected} = \beta_{measured} - \beta_{instrumental}$. The refinements were carried out using the General Structure Analysis System (GSAS/EXGUI) software package.[42] In addition, the Williamson−Hall (W−H) method was used to assess the crystallite size and lattice strain to peak broadening. The W−H relation is given by[43]

$$\beta \cos\theta = \frac{K\lambda}{\langle D \rangle} + 4\langle \varepsilon \rangle \sin\theta \quad (1)$$

where θ is the Bragg angle, K is the shape factor (typically 0.9 for quasi-spherical crystallites), and λ = 1.540 Å is the wavelength of the incident X-ray (Cu Kα radiation). In this model, the intercept of the linear fit yields $\langle D \rangle$, while the slope provides $\langle \varepsilon \rangle$ contribution (Supporting Information: Williamson−Hall plot for SnO_2 nanocrystals varying Cu concentration, Figure S5). The results indicate that Cu doping leads to both a size reduction and an increase in residual strain, consistent with the observed peak broadening. The extracted values are summarized in Table II. Analysis of the diffraction patterns indicates a decrease in the average crystallite size from approximately 9.5 to 7.0 nm as the doping level increases from 0 to 10%. A similar trend has been consistently reported across a wide range of doped systems, suggesting that this behavior is generally independent of both the dopant type and the host matrix. This observation implies that reduction in particle size, or modification of structural properties, is a general feature of the doping process, likely driven by common mechanisms such as dopant segregation at particle surfaces.[17,19,44−48] Specifically, excess dopant ions can accumulate at particle surfaces, lowering the surface energy and, thereby, reducing the final particle size. Regarding the lattice strain extracted from the XRD data, $\langle \varepsilon \rangle$, no clear trend was observed from the analysis.

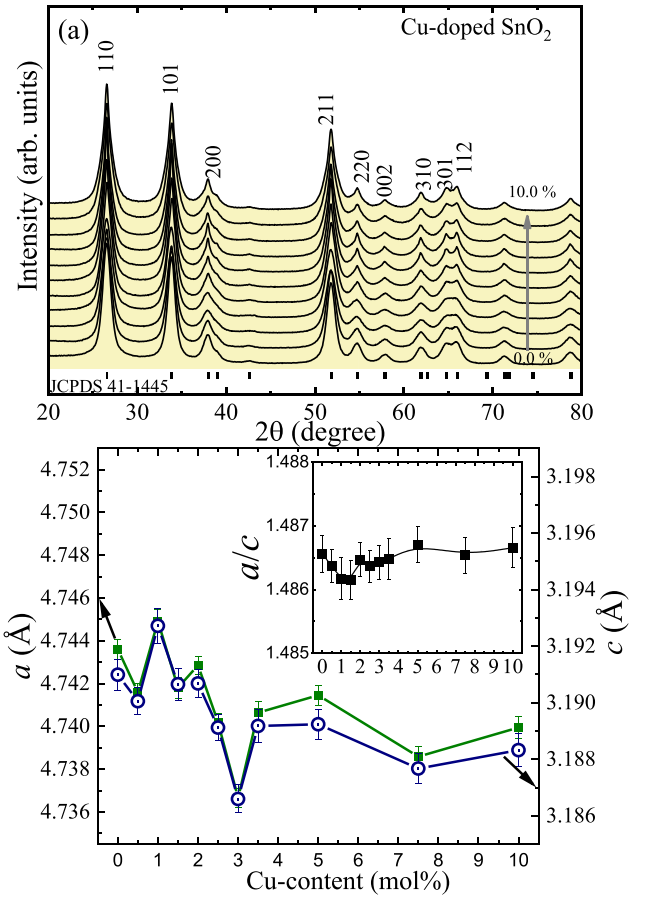

Figure 4. (a) XRD patterns of undoped and Cu-doped SnO_2 nanoparticles. (b) Lattice constants a and c as a function of copper content, with the a/c ratio also displayed, in the inset, as a function of copper content.

The lattice constants of the undoped SnO_2 nanoparticles are $a = b$ = 4.7436 and c = 3.1910 Å. As the Cu-content increases, there is a noticeable trend of the unit cell lattices to narrow, as displayed in Figure 4(b). This phenomenon may be attributed to the incorporation of Cu^{2+} ions, which, in a low-spin state, have an ionic radius of 0.54 Å, into a solid solution with Sn^{4+} ions, which have a larger ionic radius of 0.69 Å.[49] This interaction occurs within a six-coordination geometry. A solid

https://doi.org/10.1021/acs.jpcc.5c05607
J. Phys. Chem. C 2026, 130, 1257−1270

Table II. Structural Parameters of Cu-Doped SnO_2 Nanocrystals Determined by Rietveld Refinement[a]

Cu-content (mol %)	a (Å)	c (Å)	a/c	$\langle D \rangle$ (nm)	$\langle \varepsilon \rangle$ (%)
0	4.7436 (5)	3.1910 (5)	1.4866 (3)	9.5	0.09
0.5	4.7416 (4)	3.1901 (5)	1.4864 (3)	8.7	0.10
1	4.7449 (5)	3.1927 (6)	1.4862 (3)	7.5	0.12
1.5	4.7418 (5)	3.1907 (6)	1.4862 (3)	7.4	0.12
2	4.7429 (4)	3.1907 (5)	1.4865 (3)	8.3	0.08
2.5	4.7402 (4)	3.1891 (5)	1.4864 (2)	8.2	0.08
3	4.7367 (4)	3.1866 (5)	1.4864 (3)	9.0	0.08
3.5	4.7406 (5)	3.1892 (6)	1.4865 (3)	8.6	0.03
5	4.7415 (5)	3.1892 (5)	1.4867 (3)	8.1	0.10
7.5	4.7386 (5)	3.1877 (5)	1.4865 (3)	7.0	0.11
10	4.7399 (5)	3.1883 (6)	1.4867 (3)	7.2	0.06

[a]The table lists the lattice constants a and c, the axial ratio a/c, the average crystallite size $\langle D \rangle$, and the mean residual strain $\langle \varepsilon \rangle$.

solution is clearly formed, as evidenced by the systematic reduction in the lattice constants with increasing copper content. Besides, the inset in Figure 4(b) demonstrates a relatively stable a/c ratio, with minor fluctuations up to 10% doping, suggesting that incorporation of Cu into SnO_2 does not drastically alter the overall tetragonal symmetry of the lattice.

In addition, XRD findings, including preservation of (110) plane characteristics at the nanoparticle's surface, the systematic reduction of the lattice constants while preserving the a/c ratio, and preservation of the overall tetragonal lattice symmetry, are consistent with the deep in-plane (dIp) positioning of the Cu doping atoms. This comment aligns with the discussion regarding the total magnetization (M_T) calculations of both $1Cu_{Sn}(dIp)$ and $2Cu_{Sn}(dIp)$ configurations collected in Table I.

Figure 5(a,b) presents TEM images of the 2.5 and 10% Cu-doped SnO_2 NPs, respectively. The average crystalline sizes were determined by measuring approximately 400 nanoparticles from images similar to those shown in panels (a) and (b). The particle size distribution was analyzed using a log-normal fit to the frequency distribution of nanoparticle sizes, which was constructed following Sturges' method.[45] The analysis reveals a clear reduction in particle size with increasing copper doping, consistent with the results obtained from XRD measurements. Particularly, for the 2.5% Cu-doped SnO_2 nanoparticles, the average size was 8.3 ± 0.1 nm with a polydispersity index σ of 0.26 ± 0.02. In contrast, for the 10% Cu-doped SnO_2 nanoparticles, the average size decreased to 6.4 ± 0.1 nm, and σ = 0.25 ± 0.01.

Figure 5(c,d) displays the high-resolution TEM (HRTEM) images of Cu-doped SnO_2 nanoparticles for the Cu-content of 2.5 and 10.0%, respectively. Both images reveal well-defined lattice fringes with an interplanar spacing of 0.33 Å, corresponding to the (110) plane. The red markers indicate the measured d-spacing. Panels (e) and (f) display the Fourier transforms of the HRTEM images for the 2.5 and 10.0% Cu-doped SnO_2 nanoparticles, respectively. The resulting diffraction rings are indexed to the (101), (110), (200), and (211) planes of SnO_2, confirming the crystalline structure, with

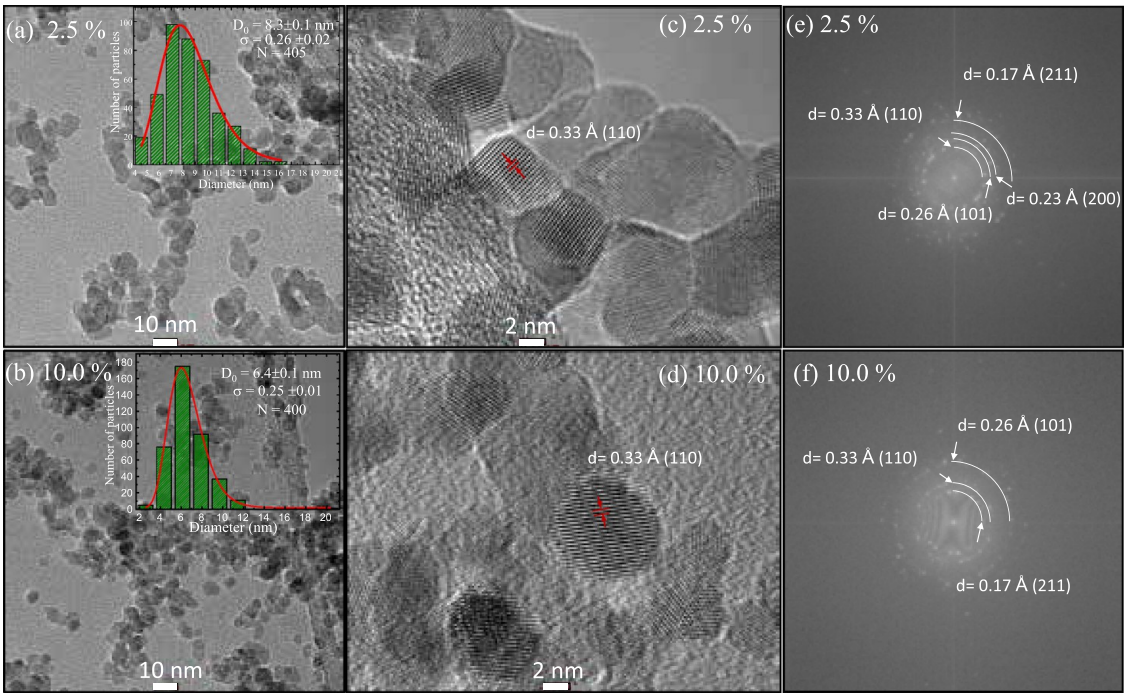

Figure 5. (a, b) TEM images for 2.5% and 10.0% Cu-content, respectively. Insets provide the particle size histograms with corresponding log-normal analyses. (c, d) HRTEM images for 2.5 and 10.0% Cu-doped SnO_2, revealing lattice fringes with an interplanar spacing of 0.33 Å corresponding to the (110) plane. (e, f) Fourier transforms of the HRTEM images, with diffraction rings indexed to the (101), (110), (200), and (211) planes, confirming the crystalline structure of SnO_2.

https://doi.org/10.1021/acs.jpcc.5c05607
J. Phys. Chem. C 2026, 130, 1257−1270

interplanar spacings of 0.33, 0.26, 0.23, and 0.17 Å, respectively.

V.II. DC Magnetic Characterization. Figure 6 shows the DC magnetic susceptibility as a function of temperature for an

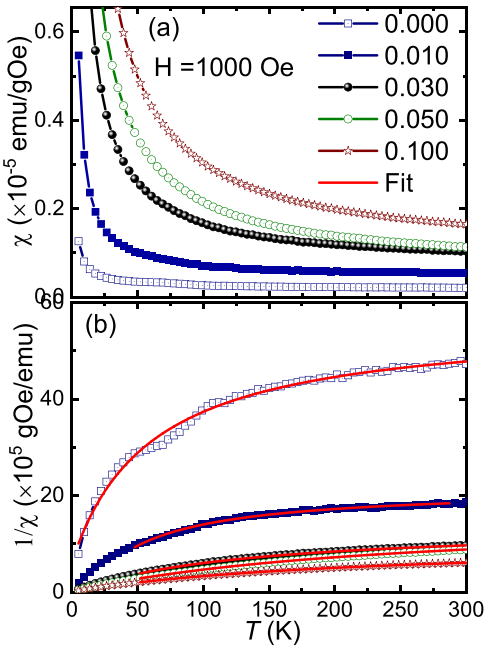

Figure 6. DC magnetic susceptibility (χ_{DC}) plotted as a function of temperature (T) for Cu-doped SnO_2 nanoparticles. Experimental data are denoted by symbols, while solid lines illustrate the fits to the Curie–Weiss law.

external magnetic field of 1 kOe, for representative samples such as undoped, 1, 3, 5, and 10% Cu-doped SnO_2 NPs. As depicted in Figure 6(a), the χ_{DC} vs T curves exhibit a consistent paramagnetic behavior across all doped samples. The temperature dependence of χ_{DC} is effectively described by the Curie–Weiss (CW) law, expressed as eq 2.

$$\chi_{DC} = C/(T - \theta_{CW}) + \chi_0 \quad (2)$$

reordering

$$\chi_{DC}^{-1} = \frac{T - \theta_{CW}}{\chi_0(T - \theta_{CW}) + C} \quad (3)$$

Here, χ_0 denotes a temperature-independent paramagnetic contribution, θ_{CW} represents the Curie–Weiss temperature, C is the Curie constant given by $C = N\mu_{eff}^2/3k_B$, N signifies the number of magnetic ions, and μ_{eff} denotes the effective magnetic moment.

It is important to note that, instead of fitting the χ_{DC} vs T data, the Curie–Weiss law was applied to the χ_{DC}^{-1} vs T data, as described in eq 3. This approach was chosen because chi-squared minimization algorithms tend to overemphasize low-temperature data points, where susceptibility is highest but adherence to Curie–Weiss behavior is often less reliable.[50] The fitting parameters are summarized in Table III.

In contrast to what would be expected for a bulk system, the undoped sample shows a positive susceptibility value, indicating a paramagnetic contribution. Nevertheless, because of the system's low dimension, the paramagnetic centers may be linked to the frequent occurrence of defects in those systems. The latter is consistent with experimental and

Table III. Values of the Curie Constant (C), Curie Temperature (θ_{CW}), Effective Magnetic Moment (μ_{eff}), and Susceptibility (χ_0) Obtained from the Analyses Using the Curie–Weiss Law

Cu-content (mol %)	C (×10⁻⁵) (emu K/gOe)	θ_{CW} (K) (K)	μ_{eff} (μ_B)	χ_0 (×10⁻⁷) (emu/gOe)
0.0	0.96 ± 0.09	−7 ± 1		1.78 ± 0.02
0.5	1.39 ± 0.04	13 ± 1	1.83 ± 0.03	5.62 ± 0.02
1.0	2.22 ± 0.09	12 ± 2	1.63 ± 0.03	4.63 ± 0.04
1.5	3.24 ± 0.07	9 ± 1	1.61 ± 0.02	4.46 ± 0.03
2.0	5.92 ± 0.08	1 ± 1	1.88 ± 0.01	4.96 ± 0.03
2.5	5.5 ± 0.1	13 ± 1	1.62 ± 0.02	6.17 ± 0.05
3.0	9.2 ± 0.1	2 ± 1	1.91 ± 0.01	7.26 ± 0.04
3.5	8.4 ± 0.1	8 ± 1	1.69 ± 0.01	5.02 ± 0.04
5.0	15.3 ± 0.1	−1 ± 1	1.90 ± 0.01	6.23 ± 0.05
7.5	17.2 ± 0.2	2 ± 1	1.64 ± 0.01	7.71 ± 0.03
10.0	21 ± 1	−2 ± 1	1.57 ± 0.01	9.41 ± 0.02

theoretical studies published elsewhere,[51,52] which suggest a direct correlation between the low dimensionality of d^0 oxides nanoparticles and the increase of defects with the emergence of unique magnetic properties.

The effective magnetic moment (μ_{eff}) of the 0.5% Cu-doped SnO_2 (1.83 μ_B) aligns well with the expected range for Cu^{2+} ions (2.02–1.81 μ_B), indicating a strong preference for Cu^{2+} oxidation state within the SnO_2 host lattice. This observation highlights the compatibility of the Cu ions with the SnO_2 matrix, where they predominantly stabilize in the 2+ state.

However, as shown in Figure 7, a noticeable downward trend in the effective magnetic moment is observed as the Cu-

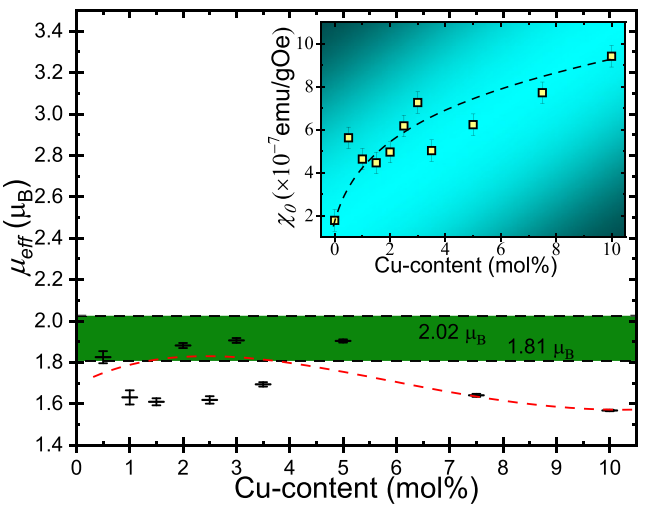

Figure 7. Effective magnetic moment (μ_{eff}) as a function of copper content. The inset is the temperature-independent paramagnetic contribution, χ_0, of Cu-doped SnO_2 nanoparticles. The green horizontal zone indicates the experimentally expected μ_{eff} range for isolated Cu^{2+} ions (1.81–2.02 μ_B). The dashed red line is only to guide the eye.

content increases. This behavior suggests that a fraction of the Cu^{2+} ions participate in interactions beyond those characteristic of the paramagnetic phase. These interactions likely contribute to a reduction in the overall magnetic moment, possibly due to ferromagnetic coupling or other forms of spin interactions within the matrix, as will be discussed later. It is

https://doi.org/10.1021/acs.jpcc.5c05607
J. Phys. Chem. C 2026, 130, 1257–1270

also important to note that ions in the paramagnetic phase may exhibit weak interactions, as suggested by the nonzero Curie–Weiss temperature. In particular, at lower concentrations, the system exhibits high and positive values, indicating a ferromagnetic interaction. However, as Cu-content increases, these values show a decreasing trend, eventually approaching small or even negative values. This transition could reflect a shift in the nature of the magnetic correlations, possibly influenced by changes in exchange interactions as the number of copper ions increases. An intriguing observation emerges from the notable and clear enhancements in the susceptibility of the temperature-independent paramagnetic contribution, denoted as χ_0 (see the inset of Figure 7). This increase is directly associated with an increase in doping content, a phenomenon that has been ascribed to Pauli paramagnetism or van Vleck paramagnetism, as suggested in the existing literature.[50]

It is important to highlight at this point that different locations are affected by copper ions during the doping process. Doping mostly causes the entrance of copper ions, which form a solid solution at lower concentrations. However, copper tends to accumulate at the surface and/or in the bulk as doping concentrations rises. This finding offers a fascinating direction for additional investigation within the theoretical framework, as pointed out in the theoretical sections.

Finally, a careful inspection of the effective magnetic moment data (experimental) collected in Table III suggests one to select the values corresponding to 3.5 and 7.5% Cu-content, namely, 1.69 and 1.64 Bohr magneton per atom, are close to the values of 4.2 and 8.3% (Table I). Likewise, the values extracted for the Bohr magneton per atom in Table III, corresponding to values of 3.5 and 7.5, are very close to each other. This correlation suggests that three Cu substitutional defects, roughly 4.2% in Table I (calculation) or 3.5% in Table III (experimental), are likely associated with the same scenario.

Then, this lower Cu-content scenario (below about 3%) is more likely associated with nearly noninteracting (isolated) Cu^{2+} ions, i.e., the $1Cu_{Sn}(dIp)$ configuration. Differently, when it comes to higher Cu-content (above about 3%), roughly 8.3% in Table I (calculation) or 7.5% in Table III (experimental), it is more likely that the $2Cu_{Sn}(dIp)$ configuration sets in. Indeed, the $1Cu_{Sn}(dIp)$ and $2Cu_{Sn}(dIp)$ configurations collected in Table I provide similar values for the total magnetic moment as the 3.5 and 7.5% Cu-contents in Table III do for the effective magnetic moment. Moreover, the reduction trend observed in Figure 7 for the effective magnetic moment as the Cu-content increases aligns with the evolution of a scenario dominated by the $1Cu_{Sn}(dIp)$ configuration (below about 3%) toward a scenario dominated by the $2Cu_{Sn}(dIp)$ configuration (above about 3%), with the latter accounting for copper clustering within the hosting SnO_2 matrix.

Figure 8(a) shows the relationship between magnetization (M) and the applied magnetic field (H) for selected samples, demonstrating a clear room-temperature ferromagnetic (RTFM) behavior. This was observed after removing the paramagnetic contribution, paramagnetism that increases as the copper content increases, as shown in the inset of Figure 8(a) for two selected values (0.02 and 0.03 Cu-content). After the paramagnetism contribution is removed, the magnetic saturation (M_S) of the ferromagnetic phase can be accurately evaluated. As displayed, the room-temperature M_S for undoped SnO_2 was determined to be approximately $\sim 7 \times 10^{-4}$, which is close to the $\sim 12 \times 10^{-4}$ emu/g reported in the literature.[17] It

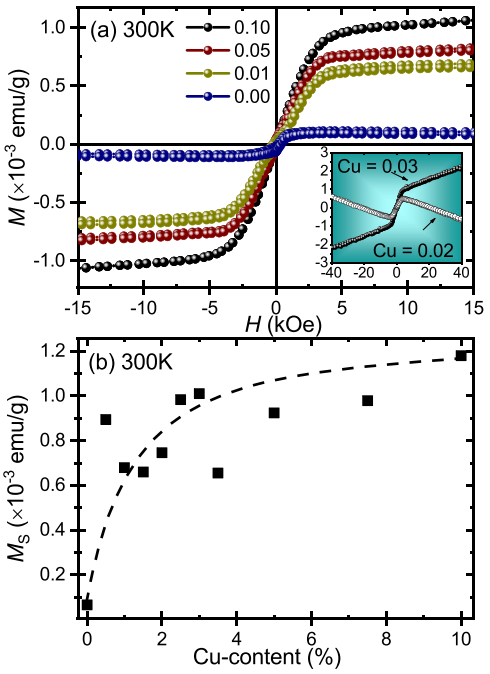

Figure 8. (a) Variation of magnetization (M) as a function of applied magnetic field (H) for selected nanoparticles. The inset shows two typical raw data for samples with 2 and 3% Cu-content. (b) Relationship between magnetic saturation (M_S) and copper content, for the undoped and Cu-doped samples SnO_2. The dashed black line is to guide the eye.

is important to mention that these values are typical for nonmagnetic oxides, generally on the order of $\times 10^{-3} - \times 10^{-4}$ emu/g.[17]

Besides, as the level of doping is heightened, all values of M_S surpass those of the undoped sample. However, there is a subtle tendency to increase M_S as the concentration of copper ions rises. This phenomenon is not readily intuitive and will be discussed in greater detail in the context of the following analysis.

A pronounced increase in the paramagnetic signal is observed in the M versus H plot, highlighting the growing enhancement of the paramagnetic response, as shown in the inset of Figure 8(a).

The M versus H loops at 5 K for the Cu-content up to 10% are depicted in Figure 9(a). All samples display paramagnetic (PM) behavior, showing the pronounced responsiveness of the PM contribution at low temperatures. Furthermore, to improve our understanding of the magnetic component, we conducted a detailed analysis of the M versus H loops using the double-Brillouin function model, given by the following equation:[19,20]

$$M = N_{\text{eff}} J_{\text{eff}} g_{\mu_B} B(y_1) + N_{\text{pol}} J_{\text{pol}} g_{\mu_B} B(y_2) \quad (4)$$

The expressions $B(y_1)$ and $B(y_2)$ denote Brillouin functions, where $y_1 = g\mu_B J_{eff} H/k_B T$ and $y_2 = g\mu_B J_{pol} H/k_B T$. In eq 4, the right-hand side comprises two components. The first pertains to isolated Cu^{2+} ions and small clusters (dimers or trimers) of adjacent Cu^{2+} ions ($\uparrow\downarrow$, $\uparrow\downarrow\uparrow\cdots$), responsible for PM and short-range atomic force microscopy (AFM) coupling suggested from the M versus H at 300 K loops, respectively. The PM contribution is expressed as an effective count of magnetic specimens (N_{eff}) with an effective angular momentum (J_{eff}).

https://doi.org/10.1021/acs.jpcc.5c05607
J. Phys. Chem. C 2026, 130, 1257−1270

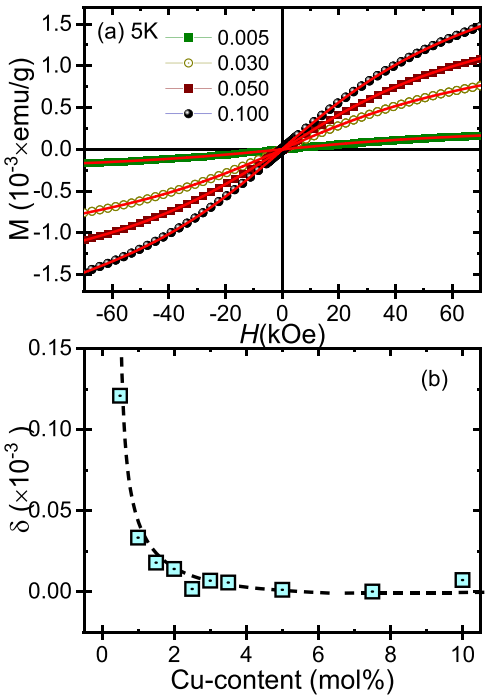

Figure 9. (a) Variation of magnetization (M) as a function of applied magnetic field (H) performed at 5 K. (b) Relationship between the polaron percolation parameter (δ) and copper content, for the Cu-doped SnO_2 samples.

The last term on the right-hand side of eq 4 corresponds to the response of the magnetic phase boundary, involving a specific number of specimens (N_{pol}) and angular momentum given by $J_{pol} = 5\nu/2$, where ($\nu = x_p\ \nu_C$). Here, x_p represents cation percolation and $\nu_C = 75$ denotes the number of cation sites for the tetragonal rutile structure of SnO_2.[20] Figure 9(a) demonstrates a robust concordance between the model and the experimental data. From this correlation, a crucial polaron percolation parameter (δ) is derived, representing a significant point on magnetic phase diagrams, as indicated in the literature.[24] In Figure 9(b), it is observed that all δ values are below the polaron percolation threshold for SnO_2 ($\delta_p = 1 \times 10^{-3}$). This observation implies that from the perspective of the bound magnetic polaron (BMP) model, the dominance of paramagnetic and clustered magnetic phases characterizes our system. In accordance with this, the formation of magnetic clusters of Cu^{2+} ions can potentially lead to the observed RTFM in the as-fabricated material. The magnetic properties of a material can be influenced by the arrangement of magnetic moments within the structure. In the context of nanoparticles doped with magnetic ions such as Cu^{2+}, the clustering of these ions can create localized regions with aligned magnetic moments.

The above-presented model picture is in agreement with the evolution of a scenario dominated by the $1Cu_{Sn}(dIp)$ configuration (below about 3% Cu-content) toward a scenario dominated by the $2Cu_{Sn}(dIp)$ configuration (above about 3% Cu-content), the latter accounting for copper clustering where short-range magnetic ordering (AFM or FM) sets in within the hosting SnO_2 matrix.

At this point, it is noteworthy to mention that the introduction of Cu^{2+} ions into a solid solution, replacing Sn^{4+} ions, may also induce formation of oxygen vacancies (V_O) as depicted by the reaction $Sn_2^{4+}O_4 \rightarrow Sn^{4+}Cu^{2+}O_3V^O$. This local defect may be accountable for the observed enhancement in the RTFM. Above about 3% Cu-content, a remarkable increase in the magnetization (M_S) by approximately 13.6 times is observed compared to the undoped SnO_2 nanoparticles, as shown in Figure 8(b).

V.III. EPR Characterization. The room-temperature EPR spectra of undoped and Cu-doped SnO_2 nanocrystals, with Cu concentrations ranging from 0 to 10%, are presented in Figure 10(a).

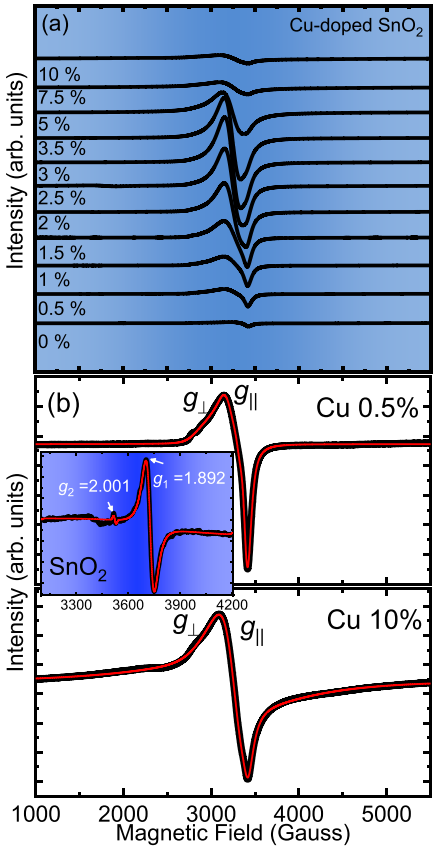

Figure 10. (a) Electron paramagnetic resonance (EPR) spectra of Cu-doped SnO_2 nanocrystals with varying Cu-content at room temperature, showing the evolution of EPR signals as a function of Cu doping concentration. (b) Fits of the undoped sample (inset), 0.5 and 10% Cu-doped SnO_2 nanocrystal.

A straightforward inspection of the spectra reveals that as the doping content increases, the resonance features become broader and more intense up to a Cu-content of 3%. Beyond this level, a decrease in signal intensity is observed, indicating potential changes in the local electronic environment and the magnetic interactions caused by Cu incorporation. To achieve a more accurate interpretation of the data, the EPR spectra were analyzed using the EasySpin software package.[53] Figure 10(b) presents typical fits for the undoped sample (inset) as well as for both 0.5 and 10% Cu-doped SnO_2. Here, the black solid line represents the experimental data, while the red continuous line corresponds to the fitted model.

For undoped SnO_2, the fitting process was carried out using three components. The primary EPR signal, with a value g_1 of 1.8922, is attributed to positively charged oxygen vacancies (V_O^+), as reported in the literature,[54] being associated with shallow defects, consistent with the observed g-tensor value.

https://doi.org/10.1021/acs.jpcc.5c05607
J. Phys. Chem. C 2026, 130, 1257−1270

The second component is identified at approximately 3520 G, corresponding to $g_2 = 2.001$, which is close to the g-factor value of 2.0023, which is typically associated with free electrons. Additionally, to achieve an accurate fit, a narrow-band component was introduced, which may be correlated with a resonance arising from spin−spin interactions. The latter could indeed be responsible for the magnetic response observed in the undoped sample (Section V.II).

In addition, incorporation of copper ions into the system induces the appearance of a distinct EPR signal characteristic of Cu^{2+} ions. This signal can be effectively analyzed using the axial spin Hamiltonian, as described in eq 5.[55]

$$H = g_{\parallel}\mu_B B_z S_z + g_{\perp}\mu_B (B_x S_x + B_Z S_y) + A_{\parallel} S_z I_z + A_{\perp}(S_x I_x + S_Z I_y) \quad (5)$$

where $g_{\parallel}$ and $g_{\perp}$ are parallel and perpendicular components of the g factor, respectively, S is the spin quantum number, I is the nuclear spin quantum number, and $A_{\parallel}$ and $A_{\perp}$ are the parallel and perpendicular components of hyperfine coupling tensor A, respectively.

The observed resonance is inherently asymmetric, which is attributed to the nuclear magnetic moment of Cu^{2+} being $I = 3/2$. This property theoretically results in the hyperfine splitting of a single peak into four distinct components, arising from the interaction between the unpaired electron and the Cu^{2+} nucleus.[56] However, at room temperature, usually, this expected hyperfine splitting is not clearly resolved in the experimental spectrum. Instead, the peaks become significantly broadened, which can be attributed to various factors such as thermal agitation or spin−lattice relaxation effects. This broadening masks the individual hyperfine components, leading to the appearance of a single, broader resonance peak, as shown in Figure 10. The fitted values for all samples are summarized in Table IV.

Table IV. Spin Hamiltonian Parameters for Cu^{2+} in Cu-Doped SnO_2 NPs

Cu-content (mol %)	$g_{\parallel}$	$g_{\perp}$	$A_{\parallel}$	$A_{\perp}$
0.5	2.2805	2.1320	433.07	166.85
1.0	2.2751	2.1337	396.97	170.67
1.5	2.2339	2.1495	441.52	139.41
2.0	2.2152	2.1633	425.27	111.40
2.5	2.1990	2.1692	395.31	87.26
3.0	2.1816	2.1727	280.94	7.75
3.5	2.1841	2.1750	300.25	7.44
5.0	2.2014	2.1716	370.36	10.12
7.5	2.2108	2.1767	308.81	21.25
10.0	2.2089	2.1707	309.18	20.07

Figure 11(a) illustrates the peak-to-peak amplitude (Amp.) as a function of copper content, showing an increase in intensity up to 3% Cu. This trend suggests the monotonic incorporation of Cu^{2+} ions into the SnO_2 lattice, substituting Sn^{4+} sites. The unpaired electrons in the Cu^{2+} ions ($3d^9$ configuration) contribute to the observed paramagnetic resonance. Notably, this behavior aligns with the linear trend observed in the lattice constants obtained from the XRD analysis (Figure 4(b)). Moreover, the observed decreasing trend of the Amp. for copper content above 3% suggests the onset of Cu^{2+} ion clustering, which diminishes the number of isolated paramagnetic centers.

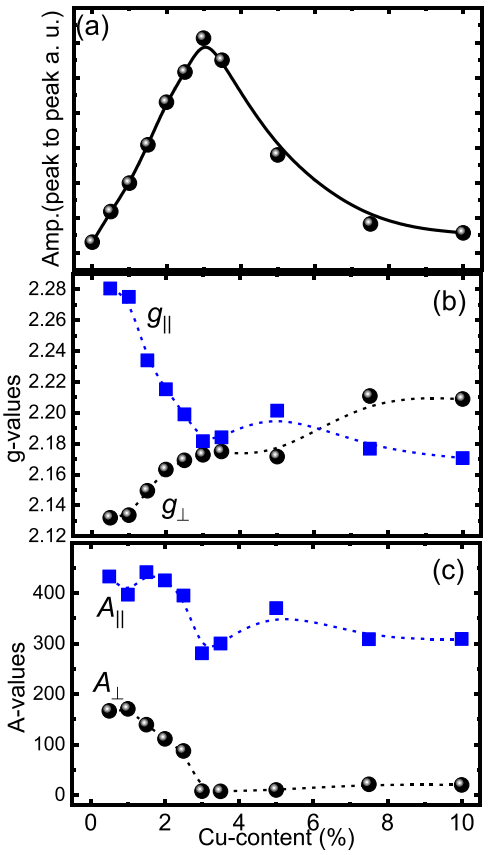

Figure 11. Evolution Hamiltonian parameters for Cu^{2+} in Cu-doped SnO_2 NPs as a function of copper content. (a) Amplitude (peak-to-peak) in arbitrary units. (b) g-Values for parallel ($g_{\parallel}$) and perpendicular ($g_{\perp}$) components. (c) Hyperfine interaction coefficients ($A_{\parallel}$ and $A_{\perp}$).

Note that this model picture aligns with the evolution of a scenario dominated by the $1Cu_{Sn}(dIp)$ configuration (below about 3% Cu-content) toward a scenario dominated by the $2Cu_{Sn}(dIp)$ configuration (above about 3% Cu-content, as discussed in Section IV).

Regarding the g-values, we first highlight the values determined for the 0.5% Cu-content, which are $g_{\parallel} = 2.2805$ and $g_{\perp} = 2.1320$. These values are consistent with those reported in the literature.[57] The observation that $g_{\parallel} > g_{\perp}$ suggests an anisotropy in the g-factor, which corresponds to isolated Cu^{2+} ions in the SnO_2 lattice. As shown in Figure 11(b), a distinct trend is observed where $g_{\parallel}$ decreases and $g_{\perp}$ increases with increasing Cu-content, suggesting that the anisotropy is reduced. This is an effect of the copper entry in the SnO_2 hosting matrix, where the electronic environment of the paramagnetic center (in this case, Cu^{2+}) changes as the dopant concentration increases. This behavior can be understood through changes in the crystal field and interactions between Cu^{2+} ions as they are incorporated into the SnO_2 lattice. The decrease in $g_{\parallel}$ suggests a weakening of the axial symmetry, possibly due to the influence of neighboring Cu ions or the formation of a more complex electronic environment.

Furthermore, the increase in $g_{\perp}$ suggests that out-of-plane interactions become more prominent with increasing Cu-content, potentially due to the emergence of Cu clustering. Additionally, the monotonic trends in $g_{\parallel}$ and $g_{\perp}$ observed in Figure 11(b) align with the Cu solid solution limit determined

https://doi.org/10.1021/acs.jpcc.5c05607
J. Phys. Chem. C 2026, 130, 1257−1270

through XRD analysis, which is approximately 3%. Again, this model picture perfectly aligns with the evolution of a scenario dominated by the $1Cu_{Sn}(dIp)$ configuration (below about 3% Cu-content) toward a scenario dominated by the $2Cu_{Sn}(dIp)$ configuration (above about 3% Cu-content), the latter accounting for copper clustering where short-range magnetic ordering (AFM or FM) sets in within the hosting SnO_2 matrix.

At doping levels higher than 3%, the g-values ($g_{\parallel}$ and $g_{\perp}$) are almost the same, as depicted in Figure 10(b). This trend can be attributed to several possible factors, such as (i) spin−spin interactions between adjacent Cu ions, as it is suggested in the Section V.II, which was responsible for reduction of the effective magnetic moment (see Figure 7), or (ii) formation of CuO or other secondary phases at higher doping levels, the former being the more likely option, as explained above. The peak in EPR intensity at 3% doping indicates an optimal concentration for maximum Cu^{2+} incorporation without significant clustering effects.

Regarding the hyperfine interaction coefficients $A_{\parallel}$ and $A_{\perp}$ for the sample with 0.5% Cu-content, their values are $A_{\parallel}$ = 433.07 and $A_{\perp}$ = 116.85. The fact that $A_{\parallel} > A_{\perp}$ indicates an axially symmetrical environment for the paramagnetic center. Furthermore, these values are higher than those typically associated with Cu^{2+} clusters, suggesting the presence of isolated Cu^{2+} ions.[58] Moreover, as the copper content increases, a rapid reduction in both $A_{\parallel}$ and $A_{\perp}$ is observed, with a significant decrease occurring up to 3% Cu-content. This behavior is likely due to the increasing influence of spin−spin interactions or clustering effects between Cu^{2+} ions, which diminish the hyperfine interaction. Interestingly, for copper concentrations above 3% and up to 10%, the values of $A_{\parallel}$ and $A_{\perp}$ remain nearly constant, suggesting that beyond a critical concentration, the local environment of the Cu^{2+} ions stabilizes, possibly due to the formation of clusters, where the hyperfine coupling is no longer sensitive to further increases in copper content.

Indeed, the trends in the g and A tensor components are very much similar and fit in the model picture of a scenario dominated by nearly isolated $1Cu_{Sn}(dIp)$ configuration (below about 3%) toward a scenario dominated by coupled $2Cu_{Sn}(dIp)$ configuration (above about 3%), as discussed in Section IV.

VI. CONCLUSIONS

In this study, we successfully synthesized high-quality Cu-doped SnO_2 nanocrystals with well-controlled doping levels and uniform incorporation of Cu^{2+} ions into the hosting crystal lattice. Electron paramagnetic resonance (EPR) data analysis revealed a clear dependence of the local electronic and magnetic environments on the Cu-content. Up to 3% Cu doping, a monotonic increase in the EPR signal intensity is observed, along with systematic changes in the g-factor anisotropy and hyperfine interaction coefficients, indicating the effective incorporation of Cu^{2+} ions substituting Sn^{4+} ions, forming a stable solid solution, consistent with magnetic measurements. Beyond 3% Cu doping, the experimental results reveal Cu^{2+} clustering and the onset of spin−spin interactions. *Ab initio* calculations show that magnetization depends strongly on the spatial arrangement of Cu ions, defect formation, and structural dimensionality. In bulk structures, the presence of oxygen vacancies and isolated Cu ions enhances magnetization, whereas 2D periodic structures exhibit higher spin polarization near surface planes. Surface atoms and near-vacuum planes contribute more to the total magnetic moment than deeper layers, and electron traps associated with oxygen vacancies further amplify the magnetization. Our combined experimental and theoretical results establish a critical doping threshold for the effective Cu^{2+} incorporation and demonstrate the tunability of SnO_2 magnetic properties via controlled heterovalent substitution and defect engineering.

■ ASSOCIATED CONTENT

Supporting Information

The Supporting Information is available free of charge at https://pubs.acs.org/doi/10.1021/acs.jpcc.5c05607.

SCHDD of the SnO2 bulk structure with one Cu atom and one oxygen vacancy; 3D bulk structure with two substitutional Cu atoms; 3D heat-map of total-, spin-up, and spin-down DOS projected on the band structure; 3D heat-map of total-, spin-up, and spin-down DOS projected on the bands structure for the slab with two copper ions; and Williamson−Hall plot for Cu-doped SnO_2 nanocrystals with varying Cu concentrations (0, 2.5, and 10%) (PDF)

■ AUTHOR INFORMATION

Corresponding Author

F. F. H. Aragón − *Instituto de Física, Universidade de Brasília, Brasília, DF 70910-900, Brazil; Departamento de Ciencias, Sección Física, Pontificia Universidad Católica del Perú, San Miguel, Lima 32, Perú;* orcid.org/0000-0001-5336-1131; Email: fherrera@unb.br, fherreraa@pucp.edu.pe

Authors

L. Villegas-Lelovsky − *São Paulo State University (UNESP), Institute of Geosciences and Exact Sciences, Rio Claro, SP 13506-900, Brazil; Physics Department, Federal University of São Carlos, São Carlos, SP 13565-905, Brazil;* orcid.org/0000-0002-3408-3612

P. C. Morais − *Centro Internacional de Física, Instituto de Física, Universidade de Brasília, Brasília, DF 70910-900, Brazil; Genomic Sciences and Biotechnology, Catholic University of Brasilia, Brasilia, DF 70790-160, Brazil*

D. G. Pacheco-Salazar − *Laboratorio de Películas Delgadas y Nanomateriales, Escuela Profesional de Física, Universidad Nacional de San Agustín, Arequipa 04000, Perú*

P. E. N de Souza − *Instituto de Física, Universidade de Brasília, Brasília, DF 70910-900, Brazil*

J.A.H. Coaquira − *Instituto de Física, Universidade de Brasília, Brasília, DF 70910-900, Brazil;* orcid.org/0000-0002-8782-6838

Ricardo Paupitz − *São Paulo State University (UNESP), Institute of Geosciences and Exact Sciences, Rio Claro, SP 13506-900, Brazil;* orcid.org/0000-0003-1254-6353

Complete contact information is available at: https://pubs.acs.org/10.1021/acs.jpcc.5c05607

Funding

The Article Processing Charge for the publication of this research was funded by the Coordenacao de Aperfeicoamento de Pessoal de Nivel Superior (CAPES), Brazil (ROR identifier: 00x0ma614).

Notes

The authors declare no competing financial interest.

■ ACKNOWLEDGMENTS

The authors acknowledge the financial support provided by the Peruvian agency CONCYTEC through contract # PE501080388-2022-PROCIENCIA, Brazilian agency Fundação de Amparo à Pesquisa do Estado de São Paulo—FAPESP for grant #2021/14977-2 and Conselho Nacional de Desenvolvimento Científico e Tecnológico—CNPq for grant #313592/2023-3. This research was partially supported by the supercomputers of Santos Dumont LNCC, CENAPAD and INKARI-IAAPP of the Universidad Nacional de San Agustín de Arequipa. F.F.H.A. acknowledges financial support from the Peruvian agency ProCiencia under project PE501087009-2024, as well as from the Air Force Office of Scientific Research (AFOSR) through Grant No. FA9550-25-1-0006.

■ REFERENCES

(1) Oka, Y.; Yanata, K.; Okamoto, H.; Takahashi, M.; Shen, J. Giant magneto-optical effects in diluted magnetic semiconductor nanostructures. *Solid-State Electron.* **1998**, *42*, 1267−1271.
(2) Furdyna, J. K. Diluted magnetic semiconductors: An interface of semiconductor physics and magnetism (invited). *J. Appl. Phys.* **1982**, *53*, 7637−7643.
(3) Dietl, T. A ten-year perspective on dilute magnetic semiconductors and oxides. *Nat. Mater.* **2010**, *9*, 965−974.
(4) Ohno, H. Making Nonmagnetic Semiconductors Ferromagnetic. *Science* **1998**, *281*, 951−956.
(5) Wolf, S. A.; Awschalom, D. D.; Buhrman, R. A.; Daughton, J. M.; von Molnár, S.; Roukes, M. L.; Chtchelkanova, A. Y.; Treger, D. M. Spintronics: A Spin-Based Electronics Vision for the Future. *Science* **2001**, *294*, 1488−1495.
(6) Dietl, T.; Ohno, H.; Matsukura, F.; Cibert, J.; Ferrand, D. Zener Model Description of Ferromagnetism in Zinc-Blende Magnetic Semiconductors. *Science* **2000**, *287*, 1019−1022.
(7) Xu, C.; Hou, J.; Pang, X.; Li, X.; Zhu, M.; Tang, B. Nanoporous PtCo and PtNi Alloy Ribbons for Methanol Electrooxidation. *Int. J. Hydrogen Energy* **2012**, *37*, 10489−10498.
(8) Ghosh, S.; Verma, P.; Cramer, C. J.; Gagliardi, L.; Truhlar, D. G. Combining Wave Function Methods with Density Functional Theory for Excited States. *Chem. Rev.* **2018**, *118*, 7249−7292.
(9) Santara, B.; Giri, P. K.; Dhara, S.; Imakita, K.; Fujii, M. Oxygen vacancy-mediated enhanced ferromagnetism in undoped and Fe-doped TiO2 nanoribbons. *J. Phys. D: Appl. Phys.* **2014**, *47*, No. 235304.
(10) Xu, W.-Z.; Ren, F.-F.; Jevtics, D.; Hurtado, A.; Li, L.; Gao, Q.; Ye, J.; Wang, F.; Guilhabert, B.; Fu, L.; Lu, H.; Zhang, R.; Tan, H. H.; Dawson, M. D.; Jagadish, C. Vertically Emitting Indium Phosphide Nanowire Lasers. *Nano Lett,* **2018**, *18*, 3414−3420.
(11) Han, G.-b.; Hu, S.-j.; Yan, S.-s.; Mei, L.-M. Oxygen vacancy induced ferromagnetism in rutile TiO2?x. *Phys. Status Solidi (RRL)* **2009**, *3*, 148−150.
(12) Kim, D.; Hong, J.; Park, Y. R.; Kim, K. J. The origin of oxygen vacancy induced ferromagnetism in undoped TiO2. *J. Phys.: Condens. Matter* **2009**, *21*, No. 195405.
(13) Peng, P.; Hu, A.; Gerlich, A. P.; Zou, G.; Liu, L.; Zhou, Y. N. Joining of Silver Nanomaterials at Low Temperatures: Processes: Properties, and Applications. *ACS Appl. Mater. Interfaces* **2015**, *7*, 12597−12618.
(14) Dev, P.; Xue, Y.; Zhang, P. Defect-Induced Intrinsic Magnetism in Wide-Gap III Nitrides. *Phys. Rev. Lett.* **2008**, *100*, No. 117204.
(15) Das Pemmaraju, C.; Sanvito, S. Ferromagnetism Driven by Intrinsic Point Defects in HfO_2. *Phys. Rev. Lett.* **2005**, *94*, No. 217205.
(16) Peng, H.; Xiang, H. J.; Wei, S.-H.; Li, S.-S.; Xia, J.-B.; Li, J. Origin and Enhancement of Hole-Induced Ferromagnetism in First-Row d^0 Semiconductors. *Phys. Rev. Lett.* **2009**, *102*, No. 017201.
(17) Aragón, F. F. H.; Coaquira, J. A. H.; Hidalgo, P.; Brito, S. L. M.; Gouvêa, D.; Castro, R. H. R. Structural and magnetic properties of pure and nickel doped SnO2 nanoparticles. *J. Phys.: Condens. Matter* **2010**, *22*, No. 496003.
(18) Aquino, J. C. R.; Aragón, F. F. H.; Coaquira, J. A. H.; Gratens, X.; Chitta, V. A.; Gonzales, I.; Macedo, W. A. A.; Morais, P. C. Evidence of Cr3+ and Cr4+ Coexistence in Chromium-Doped SnO2 Nanoparticles: A Structural and Magnetic Study. *J. Phys. Chem. C* **2017**, *121*, 21670−21677.
(19) Aragón, F. H.; Coaquira, J. A. H.; Gonzalez, I.; Nagamine, L. C. C. M.; Macedo, W. A. A.; Morais, P. C. Fe doping effect on the structural, magnetic and surface properties of SnO2 nanoparticles prepared by a polymer precursor method. *J. Phys. D: Appl. Phys.* **2016**, *49*, No. 155002.
(20) Aragón, F. H.; Chitta, V. A.; Coaquira, J. A. H.; Hidalgo, P.; Brito, H. F. Long-range ferromagnetic order induced by a donor impurity band exchange in SnO2:Er3+ nanoparticles. *J. Appl. Phys.* **2013**, *114*, No. 203902.
(21) Aquino, J. C. R.; Aragón, F. F. H.; Pacheco-Salazar, D. G.; Coaquira, J. A. H. Influence of Dy doping on the structural, vibrational, optical, electronic, and magnetic properties of SnO2 nanoparticles. *J. Nanopart. Res.* **2021**, *23*, No. 90.
(22) Sharma, M.; Aljawfi, R. N.; Kumari, K.; Chae, K. H.; Gautam, S.; Dalela, S.; Alvi, P. A.; Kumar, S. Investigation of local atomic structure of Ni doped SnO2 thin films via X-ray absorption spectroscopy and their magnetic properties. *J. Mater. Sci.: Mater. Electron.* **2019**, *30*, 760−770.
(23) Sharma, M.; Kumar, S.; Aljawfi, R. N.; Dalela, S.; Dolia, S. N.; Alshoaibi, A.; Alvi, P. A. Role of Fe-Doping on Structural, Optical and Magnetic Properties of SnO2 Nanoparticles. *J. Electron. Mater.* **2019**, *48*, 8181−8192, DOI: 10.1007/s11664-019-07649-x.
(24) Coey, J. M. D.; Venkatesan, D. M.; Fitzgerald, C. Donor Impurity Band Exchange in Dilute Ferromagnetic Oxides. *Nat. Mater.* **2005**, *4*, 173−179.
(25) Cox, D. F.; Fryberger, T. B.; Semancik, S. Oxygen vacancies and defect electronic states on the SnO2(110)-1×1 surface. *Phys. Rev. B* **1988**, *38*, 2072.
(26) Carbajal-Franco, G.; Marquez-Quintana, M. F. DFT Path Towards the Characterization of the SnO2-CH4 Gas Sensing Reactions. *MRS Advances* **2017**, *2*, 3925−3931.
(27) Trani, F.; Causa, M.; Ninno, D.; Cantele, G.; Barone, V. Density functional study of oxygen vacancies at the SnO2 surface and subsurface sites. *Phys. Rev. B.* **2008**, *77*, 245410.
(28) Rantala, T. T; Rantala, T. S; Lantto, V. Electronic structure of SnO2 (110) surface. *Materials Science in Semiconductor Processing* **2000**, *3*, 103−107.
(29) Chen, H. T.; Xiong, S. J.; Wu, X. L.; Zhu, J.; Shen, J. C.; Chu, P. K. Tin Oxide Nanoribbons with Vacancy Structures in Luminescence-Sensitive Oxygen Sensing. *Nano Lett.* **2009**, *9*, 1926−1931.
(30) Cox, P.A.; Egdell, R.G.; Harding, C.; Patterson, W.R.; Tavener, P.J. Surface properties of antimony doped tin(IV) oxide: A study by electron spectroscopy. *Surface Science* **1982**, *123*, 179−203.
(31) Hohenberg, P.; Kohn, W. Inhomogeneous Electron Gas. *Phys. Rev.* **1964**, *136*, No. B864.
(32) Kohn, W.; Sham, L. J. Self-Consistent Equations Including Exchange and Correlation Effects. *Phys. Rev.* **1965**, *140*, No. A1133.
(33) Giannozzi, P.; Baroni, S.; Bonini, N.; et al. QUANTUM ESPRESSO: a modular and open-source software project for quantum simulations of materials. *J. Phys.: Condens. Matter* **2009**, *21*, No. 395502.
(34) Giannozzi, P.; Andreussi, O.; Brumme, T.; et al. Advanced capabilities for materials modelling with QUANTUM ESPRESSO. *J. Phys.: Condens. Matter* **2017**, *29*, No. 465901.
(35) Giannozzi, P.; Baseggio, O.; Bonfà, P.; Brunato, D.; Car, R.; Carnimeo, I.; Cavazzoni, C.; de Gironcoli, S.; Delugas, P.; Ruffino, F. F.; Ferretti, A.; Marzari, N.; Timrov, I.; Urru, A.; Baroni, S. Quantum ESPRESSO toward the exascale. *J. Chem. Phys.* **2020**, *152*, No. 154105.
(36) Perdew, J. P.; Burke, K.; Ernzerhof, M. Generalized Gradient Approximation Made Simple. *Phys. Rev. lett.* **1996**, *77*, No. 3865.

https://doi.org/10.1021/acs.jpcc.5c05607
J. Phys. Chem. C 2026, 130, 1257−1270

(37) Perdew, J. P.; Burke, K.; Ernzerhof, M. Generalized Gradient Approximation Made Simple. *Phys. Rev. Lett.* **1996**, *77*, No. 1396.
(38) Blöchl, P. E. Projector Augmented−Wave Method. *Phys. Rev. B* **1994**, *50*, No. 17953.
(39) Kresse, G.; Joubert, D. From Ultrasoft Pseudopotentials to the Projector Augmented-Wave Method. *Phys. Rev. B* **1999**, *59*, No. 1758.
(40) Dimesso, L. *Handbook of Sol-Gel Science and Technology*; Klein, L.; Aparicio, M.; Jitianu, A., Eds.; Springer International Publishing: Cham, 2016; pp 1−22.
(41) Aragón, F.; Coaquira, J.; Hidalgo, P.; Brito, S.; Gouvêa, D.; Castro, R. Experimental study of the structural, microscopy and magnetic properties of Ni-doped SnO2 nanoparticles. *J. Non-Cryst. Solids* **2010**, *356*, 2960−2964.
(42) Larson, A.; Dreele, R.; Toby, B. General structure analysis system - GSAS/EXPGUI. *j. Appl. Cryst.* **1994**, *748*, No. 544.
(43) Dangi, S.; Hashmi, S.; Kumar, U.; Choudhary, B.; Kuznetsov, A.; Dalela, S.; Kumar, S.; Dolia, S.; Kumar, S.; Sofi, B. F.; Darwesh, R.; Hasan, P.; Alvi, P. Exploration of spectroscopic, surface morphological, structural, electrical, optical and mechanical properties of biocompatible PVA-GO PNCs. *Diamond Relat. Mater.* **2022**, *127*, No. 109158.
(44) Castro, R. H.; Hidalgo, P.; Muccillo, R.; Gouvêa, D. Microstructure and structure of NiO−SnO2 and Fe2O3−SnO2 systems. *Appl. Surf. Sci.* **2003**, *214*, 172−177.
(45) Aragón, F. F. H.; Coaquira, J. A. H.; Villegas-Lelovsky, L.; da Silva, S. W.; Cesar, D. F.; Nagamine, L. C. C. M.; Cohen, R.; Menéndez-Proupin, E.; Morais, P. C. Evolution of the doping regimes in the Al-doped SnO2 nanoparticles prepared by a polymer precursor method. *J. Phys.: Condens. Matter* **2015**, *27*, No. 095301.
(46) Coelho-Júnior, H.; Aquino, J. C. R.; Aragón, F. H.; Hidalgo, P.; Cohen, R.; Nagamine, L. C. C. M.; Coaquira, J. A. H.; da Silva, S. W.; Brito, H. F. Doping effects on the structural, magnetic, and hyperfine properties of Gd-doped SnO2 nanoparticles. *J. Nanopart. Res.* **2014**, *16*, No. 2689.
(47) Aragón, F.; Morais, P.; Souza, P.; da Silva, S. Defect dynamics evolution in Zn1-xAlxO nanocrystals: Interplay of structural, optical, and electrical properties. *J. Alloys Compd.* **2025**, *1039*, No. 183020.
(48) Aragón, F. F. H.; Aquino, J. C. R.; Ramos, J. E.; Coaquira, J. A. H.; Gonzalez, I.; Macedo, W. A. A.; da Silva, S. W.; Morais, P. C. Fe-doping effects on the structural, vibrational, magnetic, and electronic properties of ceria nanoparticles. *J. Appl. Phys.* **2017**, *122*, No. 204302.
(49) Shannon, R. D. Revised effective ionic radii and systematic studies of interatomic distances in halides and chalcogenides. *Acta Crystallogr., Sect. A* **1976**, *32*, 751−767.
(50) Mugiraneza, S.; Hallas, A. Tutorial: a beginner's guide to interpreting magnetic susceptibility data with the Curie-Weiss law. *Commun. Phys.* **2022**, *5*, No. 95.
(51) Sundaresan, A.; Bhargavi, R.; Rangarajan, N.; Siddesh, U.; Rao, C. N. R. Ferromagnetism as a universal feature of nanoparticles of the otherwise nonmagnetic oxides. *Phys. Rev. B* **2006**, *74*, No. 161306.
(52) Luitel, H.; Chettri, P.; Tiwari, A.; Sanyal, D. Experimental and first principle study of room temperature ferromagnetism in carbon-doped rutile TiO2. *Mater. Res. Bull.* **2019**, *110*, 13−17.
(53) Stoll, S.; Schweiger, A. EasySpin, a comprehensive software package for spectral simulation and analysis in EPR. *J. Magn. Reson.* **2006**, *178*, 42−55.
(54) Thiyagarajan, K.; Sivakumar, K. Oxygen vacancy-induced room temperature ferromagnetism in graphene-SnO2 nanocomposites. *J. Mater. Sci.* **2017**, *52*, 8084−8096.
(55) Silva, A. S.; Pelegrini, F.; Figueiredo, L. C.; de Souza, P. E.; Morais, P. C.; Dantas, N. O. Effects of Cu2+ ion incorporation into ZnTe nanocrystals dispersed within a glass matrix. *J. Alloys Compd.* **2018**, *749*, 681−686.
(56) Gala, L.; Lawson, M.; Jomova, K.; Zelenický, L.; Congradyova, A.; Mazur, M.; Valko, M. EPR Spectroscopy of a Clinically Active (1:2) Copper(II)-Histidine Complex Used in the Treatment of Menkes Disease: A Fourier Transform Analysis of a Fluid CW-EPR Spectrum. *Molecules* **2014**, *19*, 980−991.
(57) Anitha, B.; Khadar, M. A. Dopant concentration dependent magnetism of Cu-doped TiO2 nanocrystals. *J. Nanopart. Res.* **2016**, *18*, No. 149.
(58) Cordoba, G.; Viniegra, M.; Fierro, J.; Padilla, J.; Arroyo, R. TPR, ESR, and XPS Study of Cu2+Ions in Sol−Gel-Derived TiO2. *J. Solid State Chem.* **1998**, *138*, 1−6.

https://doi.org/10.1021/acs.jpcc.5c05607
J. Phys. Chem. C 2026, 130, 1257−1270